

Plume-induced topography and geoid anomalies and their implications for the Tharsis rise on Mars

James H. Roberts

Department of Astrophysical and Planetary Sciences, University of Colorado, Boulder, Colorado, USA

Shijie Zhong

Department of Physics, University of Colorado, Boulder, Colorado, USA

Received 15 December 2003; revised 11 February 2004; accepted 17 February 2004; published 20 March 2004.

[1] The topography and geoid anomalies produced from an upwelling plume are sensitive to the depth of plume buoyancy, D_p , and elastic lithospheric thickness, T_e , both of which control the degree of compensation. We formulated spherically axisymmetric convection models of mantle plumes with temperature- and pressure-dependent viscosity to dynamically determine D_p and T_e and the resulting topography and geoid anomalies from the plume. From 10 cases with different Rayleigh number, activation energy, and activation volume, we determined T_e ranging from 100 km to 180 km and D_p that is approximately twice T_e . The ratio of geoid to topography, $R_{G/T}$, from these plume models is either negative or slightly positive (<0.03) at wavelengths that are most relevant to the Tharsis rise (low harmonics from degrees 2 to 4). The modeled $R_{G/T}$ is significantly smaller than that observed for the Tharsis rise, suggesting that Tharsis is unlikely to be dynamically supported.

INDEX TERMS: 8122 Tectonophysics: Dynamics, gravity and tectonics; 5430 Planetology: Solid Surface Planets: Interiors (8147); 5417 Planetology: Solid Surface Planets: Gravitational fields (1227); 5475 Planetology: Solid Surface Planets: Tectonics (8149); 5480 Planetology: Solid Surface Planets: Volcanism (8450); **KEYWORDS:** geoid, Martian geophysics, Tharsis

Citation: Roberts, J. H., and S. Zhong (2004), Plume-induced topography and geoid anomalies and their implications for the Tharsis rise on Mars, *J. Geophys. Res.*, 109, E03009, doi:10.1029/2003JE002226.

1. Introduction

[2] The long wavelengths of topography and geoid on Mars are dominated by the Tharsis rise [Zuber and Smith, 1997], causing a very high correlation between topography and geoid at long wavelengths [McGovern *et al.*, 2002]. Two different models have been proposed to explain the long-wavelength elevated topography associated with the Tharsis rise. Topography may be created dynamically by a buoyant mantle plume pushing the lithosphere up from below [Harder and Christensen, 1996]. Alternately, the topography may be a volcanic construction which is only partially compensated [Turcotte *et al.*, 1981; Phillips *et al.*, 2001]. More recent studies suggest another possibility: that the thermal anomaly responsible for Tharsis was induced by a giant impact, rather than convection [Reese *et al.*, 2002].

[3] The dynamic topography model requires that a single large plume persists in the Martian mantle, centered under the Tharsis region. Smaller plumes may exist elsewhere (e.g., under Elysium), but do not contribute any significant buoyancy at long wavelengths. The geoid and topography anomalies associated with Tharsis are dominated by the long wavelengths ($\ell \leq 4$). Plume buoyancy at such long wavelengths only exists immediately below the lithosphere

where plume materials spread horizontally. Harder and Christensen [1996] showed that a single mantle plume may be produced dynamically in 3-D convection models by including an endothermic phase change, corresponding to the 670 km transition in the Earth. The shape of the dynamic geoid is roughly consistent with the observed geoid, but only 10% of the magnitude. By using a thicker lithosphere, the plume buoyancy is forced lower and the geoid anomalies can be increased to 60% of the observed values [Harder, 2000]. However, these studies neglect the dependence of viscosity on temperature and the elastic effects of the lithosphere. The elastic effects of the lithosphere can be very important in influencing long-wavelength gravity anomalies produced by a plume [Zhong, 2002]. Phillips *et al.* [2001] considered the Tharsis rise to be a surface load on a spherical elastic shell with a thickness of 100 km. Their predictions of the shape and magnitudes of the gravity anomalies are consistent with the observations up to degree 10.

[4] Studies simultaneously considering internal and surface loading of an elastic lithosphere suggest that the plume buoyancy cannot be responsible for more than 15% of the long-wavelength ($\ell = 2-4$) geoid or 25% of the long-wavelength topography provided that the elastic thickness, $T_e < 200$ km [Zhong and Roberts, 2003]. However, the estimates depend on T_e and D_p , the depth at which long-wavelength plume buoyancy is located. Zhong and Roberts

[2003] estimated T_e and D_p on the basis of scaling arguments. A better understanding of T_e and D_p and their effects on plume-induced geoid is essential if we want to constrain the plume's contribution to the Tharsis geoid and topography. In addition, it is important to include temperature-dependent viscosity in convection models of dynamic topography and geoid [King and Hager, 1994]. In this work, by formulating models of thermal plumes with temperature- and depth-dependent viscosity, we dynamically determine D_p and T_e , and investigate the relationship between those parameters. We also examine the dynamic topography and geoid that the plume buoyancy may produce by considering the elastic filtering effect, using T_e determined from the dynamic models.

[5] We organize this paper as follows. We will first present the modeling procedures, including the convection models, the rheology and the elastic filtering. Second, we will show the results of T_e and D_p from these calculations and investigate the effects of T_e and D_p on the long-wavelength geoid. We conclude with a discussion of the implications of these results for the support of Tharsis.

2. Model Descriptions

[6] The modeling was broken into three different phases. First, we performed a series of convection calculations with the goal of producing plumes in a physically realistic mantle. We determined T_e and D_p from each of the models. Buoyancy forces associated with the plume create topography at the surface and core-mantle boundary. However the presence of an elastic lithosphere at the surface creates membrane stresses that oppose the buoyancy forces. This opposing stress serves to reduce the dynamic topography produced by the plume buoyancy [Zhong, 2002]. In the second phase, we quantified the topographic reduction due to these elastic effects. We treated the lithosphere as an elastic shell of thickness T_e , applied the plume-induced surface topography from the convection models as a load to this shell, and determined the resulting deformation (or the true topography) in response to this load and to the elastic stresses [Turcotte et al., 1981; Zhong, 2002]. In the final phase of the modeling, we calculated the geoid anomalies due to the topography at the surface and CMB and the convective thermal structure, including the plume.

[7] The mantle is heated both from below and from within and cooled from above. Mantle convection can be described by the conservation equations of mass, momentum and energy. Assuming an incompressible mantle and using the Boussinesq approximation, the nondimensionalized governing equations are

$$\nabla \cdot \vec{u} = 0, \quad (1)$$

$$-\nabla P + \nabla \cdot [\eta(\nabla \vec{u} + \nabla^T \vec{u})] + RaT\vec{e}_r = 0, \quad (2)$$

$$\frac{\partial T}{\partial t} + \vec{u} \cdot \nabla T = \nabla^2 T + \gamma, \quad (3)$$

where \vec{u} is the velocity, P is the pressure, T is the temperature, and γ is the rate of internal heat production.

Table 1. Model Parameters

Parameter	Value
Planetary radius	3400 km
Core radius	1400 km
Crustal thickness	50 km
Gravitational acceleration	3.73 m s ⁻²
Mantle density	3500 kg m ⁻³
Core density	7000 kg m ⁻³
Crustal density	2900 kg m ⁻³
Young's modulus	1.4 × 10 ¹¹ Pa
Thermal diffusivity	10 ⁻⁶ m ² s ⁻¹
Thermal expansivity	3 × 10 ⁻⁵ K ⁻¹
Specific heat	1200 J K ⁻¹ kg ⁻¹
Temperature difference	1440 K
Surface temperature	220 K
Viscosity cutoff	10 ⁶

Adiabatic heating is neglected in the heat equation. The Rayleigh number, Ra , is defined as

$$Ra = \frac{\rho_0 g \alpha \Delta T R_0^3}{\kappa \eta_0}, \quad (4)$$

where ρ_0 is the reference density of the mantle, R_0 is the radius of the planet, α is the thermal expansivity, ΔT is the temperature change across the mantle, κ is the thermal diffusivity, and η_0 is the reference viscosity. In this case, the reference viscosity is that at the bottom of the mantle. The nondimensional internal heating rate is given by

$$\gamma = \frac{QR_0^2}{\rho_0 C \Delta T \kappa}, \quad (5)$$

where Q is the internal heating rate measured as energy per time per volume, and C is the specific heat. Note that we use the radius of the planet as the characteristic length scale in all nondimensionalizations, rather than the thickness of the convecting mantle. Our Rayleigh numbers will therefore be a factor of 4.9 higher than those in comparable cases which normalize to the mantle thickness (see Table 1 for model parameters).

[8] The isothermal and free-slip boundary conditions are applied at both the surface and the core-mantle boundary. We used an initial temperature profile consistent with that of a convecting mantle. The interior was initially isothermal at 1300 K. The temperature in the boundary layers at the top and bottom changed linearly with radius to match up with the isothermal boundary conditions.

[9] We use a temperature- and depth-dependent rheology, following an Arrhenius law. The nondimensional viscosity, η is given by

$$\eta = \exp \left[\frac{E' + V'(1-r)}{T + T_s} - \frac{E' + V'(1-r_{core})}{1 + T_s} \right], \quad (6)$$

using the following normalizations:

$$E' = \frac{E}{R\Delta T}, \quad V' = \frac{\rho_0 g R_0 V}{R\Delta T}, \quad T_s = \frac{T_0}{\Delta T}, \quad (7)$$

where E is the activation energy, V is the activation volume, R is the gas constant, r is the radial position, r_{core} is the core

Table 2. Parameters for Convection Calculations

Case	Ra	E, kJ/mol	V, cm ³ /mol	Q, W/m ³	T _e , km	D _p , km	R _{G/T} (ℓ = 2)
1	5 × 10 ⁸	150	2.5	5 × 10 ⁻⁹	159	269	-0.0348
2	5 × 10 ⁸	150	3	5 × 10 ⁻⁹	147	269	-0.0412
3	5 × 10 ⁸	150	3.5	5 × 10 ⁻⁹	111	193	-0.0433
4	5 × 10 ⁸	150	4	5 × 10 ⁻⁹	105	172	-0.0658
5	5 × 10 ⁸	120	3	5 × 10 ⁻⁹	104	172	-0.0309
6	5 × 10 ⁸	180	3	5 × 10 ⁻⁹	180	314	-0.0450
7	5 × 10 ⁸	150	3	5 × 10 ⁻⁹	132	234	-0.0323
8	5 × 10 ⁸	150	3	0	150	249	-0.0395
9	2 × 10 ⁸	150	3	5 × 10 ⁻⁹	174	294	-0.0430
10	1 × 10 ⁹	150	3	5 × 10 ⁻⁹	118	180	-0.0344

radius, and T_s is the nondimensional surface temperature. η has been normalized to the viscosity at the CMB.

[10] A finite-element convection code, Citcom [Moresi and Solomatov, 1995; Moresi and Gurnis, 1996], was modified to solve these governing equations (1)–(3) in axisymmetric spherical geometry [Zhong, 2002]. The equations were solved on a grid of 128 evenly spaced elements in latitude and 64 elements in radius, using adaptive time steps. The equations were integrated until the system reached a steady state. We classify a system as being in the steady state when the heat fluxes at the top and bottom boundaries and the horizontally averaged temperature profile stops changing with time.

[11] The calculations were performed over one hemisphere, $0 \leq \theta \leq \frac{\pi}{2}$, where θ is the co-latitude, and assumed symmetry about the equator. We made this assumption to promote the formation of a single plume, making it easier to determine D_p . However, the odd harmonics are missing due to this assumption. Because there is no degree-1 component to the geoid, degree-2 is the longest and most critical wavelength to our analysis. This $\ell = 2$ structure is adequately modeled in a single hemisphere.

[12] The viscosity of the Martian mantle is not well constrained. Therefore we experimented with a range of viscosities (2×10^{19} – 10^{20} Pa s at the CMB) corresponding to a range of Ra between 2×10^8 – 10^9 (Table 2). We have taken the temperature of the CMB to be 1950 K [Nimmo and Stevenson, 2000; Zhong and Zuber, 2001] and removed the adiabatic temperature increase with pressure to obtain a superadiabatic temperature difference of 1440 K (Table 1).

[13] Mantle convection models assume that the mantle deforms as a viscous flow and that dynamic topography is determined by the viscous normal stress at the surface and CMB [Hager and Richards, 1989; Harder and Christensen, 1996]. However, for planets with relatively thick lithosphere, significant normal stresses resulting from mantle convection may be supported by elastic stresses in the lithosphere rather than producing dynamic topography at the surface [Zhong, 2002]. This elastic filtering effect on topography can be included by applying the viscous normal stress as a load to an elastic shell [Zhong, 2002; Zhong and Roberts, 2003]. This results in a reduction of the dynamic topography compared to the purely viscous case, and has significant effects on the geoid anomalies [Zhong, 2002].

3. Results

3.1. Plume Structure

[14] Our models with temperature- and depth-dependent viscosity produce an upwelling plume at the pole (i.e., $\theta = 0$).

Figure 1a shows the steady-state thermal structure from a representative case with $Ra = 5 \times 10^8$, $E = 150$ kJ/mol, $V = 3 \times 10^{-6}$ m³/mol, and $Q = 5 \times 10^{-9}$ W/m³. A mantle plume rises along a conduit from the core-mantle boundary and spreads out beneath the stagnant lid, forming a plume head with long-wavelength structure there. Figure 1b shows the corresponding temperature spectrum at each depth. Because our convection models assumed reflection symmetry about the equator, the odd harmonics are missing. The plume is dominated by $\ell = 2$ and $\ell = 4$ at shallow depths. The plume tail at large depths contributes little power at long wavelengths. Figure 1c shows the corresponding horizontally averaged temperature and viscosity profiles. There is a minimum in viscosity at a depth of 350 km, typical for temperature- and depth-dependent rheology. This type of stratified viscosity structure favors the formation of long-wavelength structures or a single plume structure [Zhong and Zuber, 2001].

[15] This result is robust for a wide range of Rayleigh numbers, activation energy, activation volume, and internal heating rates. The 10 different cases in Table 2 all result in long-wavelength plume heads in a mantle with a reasonable interior temperature (1300 K). These cases also cover the range of reasonable T_e . Our values for activation energy are substantially lower than those determined experimentally [Karato and Wu, 1993]. Because we employ a Newtonian rheology, the activation energy may be approximated by dividing the experimental value by the stress exponent [Kiefer, 1997]. As long as the activation volume is sufficiently high ($V \geq 2.5 \cdot 10^{-6}$ m³/mol), this type of plume structure always develops. However, multiple upwellings may develop when V is small and the mantle viscosity is relatively uniform.

3.2. Plume Depth and Elastic Thickness

[16] Of particular interest are the depth to which this plume rises and the thickness of the elastic lithosphere. Although the depth of the plume controls the extent to which it will contribute to the geoid [Zhong and Roberts, 2003], the plume is distributed over a range of depths. However, for scaling purposes it is useful to consider some average depth, D_p , of the long-wavelength component of plume buoyancy. We define the demarcation between the plume head and plume tail as the depth at which the width of the plume doubles across one vertical element. We define D_p to be the geometric centroid of this plume head. D_p for cases with different rheological parameters (Table 2) ranged between 170 and 320 km (Figure 2).

[17] The thickness of the elastic lithosphere, T_e is defined as the depth to a certain isotherm, below which viscous

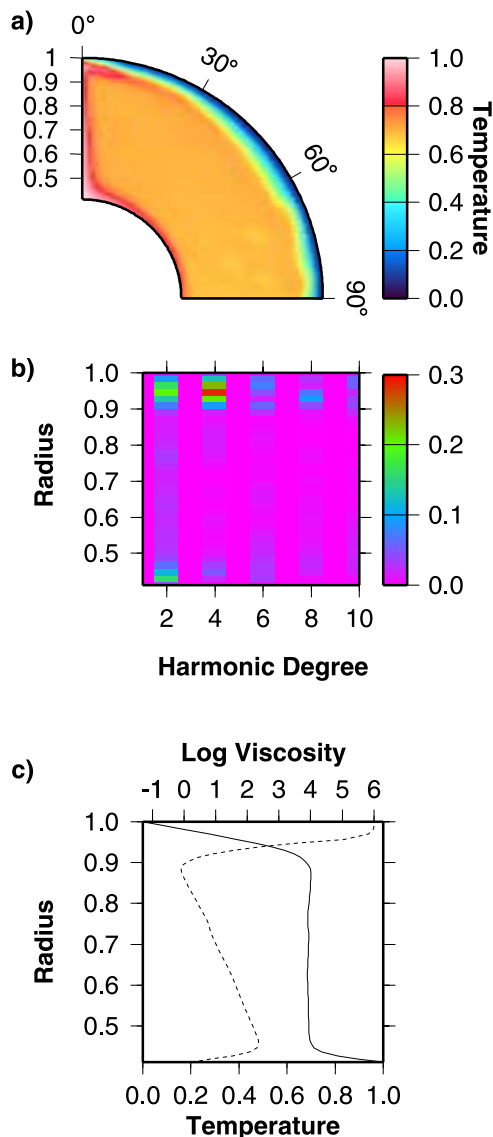


Figure 1. A long-wavelength mantle plume from a temperature- and depth-dependent viscosity convection calculation. a) Temperature profile. b) Temperature spectrum vs. depth. c) Horizontally averaged temperature (solid line) and viscosity (dashed) profiles. ($Ra = 5 \times 10^8$, $E = 150$ kJ/mol, $V = 3 \times 10^{-6}$ m³/mol, $Q = 5 \times 10^{-9}$ W/m³).

deformation dominates. Terrestrial studies [Watts *et al.*, 1980] indicate that the 500°C isotherm is appropriate. Because we are interested in long-wavelength structures, we define a global T_e as the depth at which the horizontally averaged temperature (e.g., Figure 1c) reaches 500°C. For the case in Figure 1, T_e is determined to be 147 km. T_e ranged between 100 and 180 km for our cases (circles in Figure 2), a range that is similar to those from studies of gravity and topography [Zuber *et al.*, 2001; McGovern *et al.*, 2002].

[18] T_e and D_p depend on Ra and rheological parameters in a similar way, because T_e scales with stagnant lid thickness. The base of the stagnant lid represents the shallowest depth to which a plume may rise. As convection becomes more vigorous (i.e., with larger Ra , Table 2), more

heat is transported to the top of the mantle and both the stagnant lid thickness and T_e decrease. When activation energy is increased, viscosity is more strongly dependent on temperature, causing the viscosity in the upper layers to increase. The stagnant lid thickens and T_e increases (Table 2). An increase in activation volume causes viscosity to increase more strongly with depth. Since our reference viscosity is defined as that at the bottom of the mantle, the viscosity decreases at shallow depth. This will decrease the stagnant lid thickness and T_e .

[19] Zhong and Roberts [2003] introduced a parameter β such that $D_p = \beta T_e$, and indicated that for a given T_e , a smaller β (i.e., shallower plume) causes a mantle plume to be more completely compensated, and therefore to contribute less to the geoid. Based on scaling arguments, their estimate of β is 3. Here, our numerical modeling suggests that β is 1.83 (Figure 2).

[20] The surface heat flow is, of course, higher in the region above the plume. T_e above the plume will be less than the global average. We can attempt to account for this by defining T_e as the average over the region within 45° of the plume rather than the global average. D_p still depends linearly on T_e in this case and $\beta = 2.13$ (triangles in Figure 2), which is still smaller than the prediction. If the region over which T_e is averaged is restricted to within 30° of the plume, T_e is even smaller and β increases to 2.4. A degree 2 plume structure would impinge upon a large region of the lithosphere, and therefore will be sensitive to lithospheric thickness quite some distance from the plume center. Therefore we did not attempt restricting the region in which we compute T_e any further.

[21] We have also calculated T_e as the globally averaged depth to the 450°C isotherm. This leads to reduced T_e , but the linear relation between D_p and T_e still holds. We find $\beta = 2.00$ for this case (diamonds in Figure 2). For a given convection model, D_p is the same for all three curves in

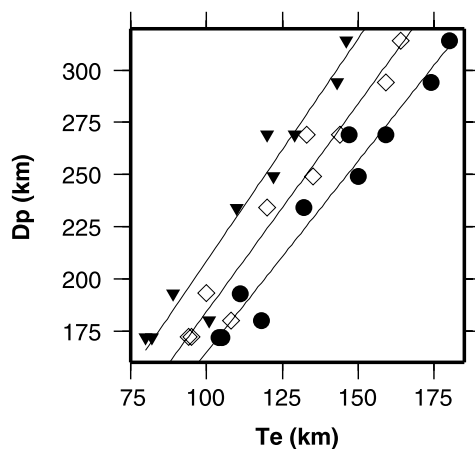


Figure 2. Plume depth vs. elastic thickness for 10 different convection models. The circles are the results for globally averaged T_e and the triangles for T_e within 45 degrees of the plume, where T_e is the depth to the 500°C isotherm. The diamonds represent the globally averaged T_e to the 450°C isotherm. The solid lines are linear fits to the points. The slope $\beta = 1.83$ for the circles, 2.13 for the triangles, and 2.0 for the diamonds.

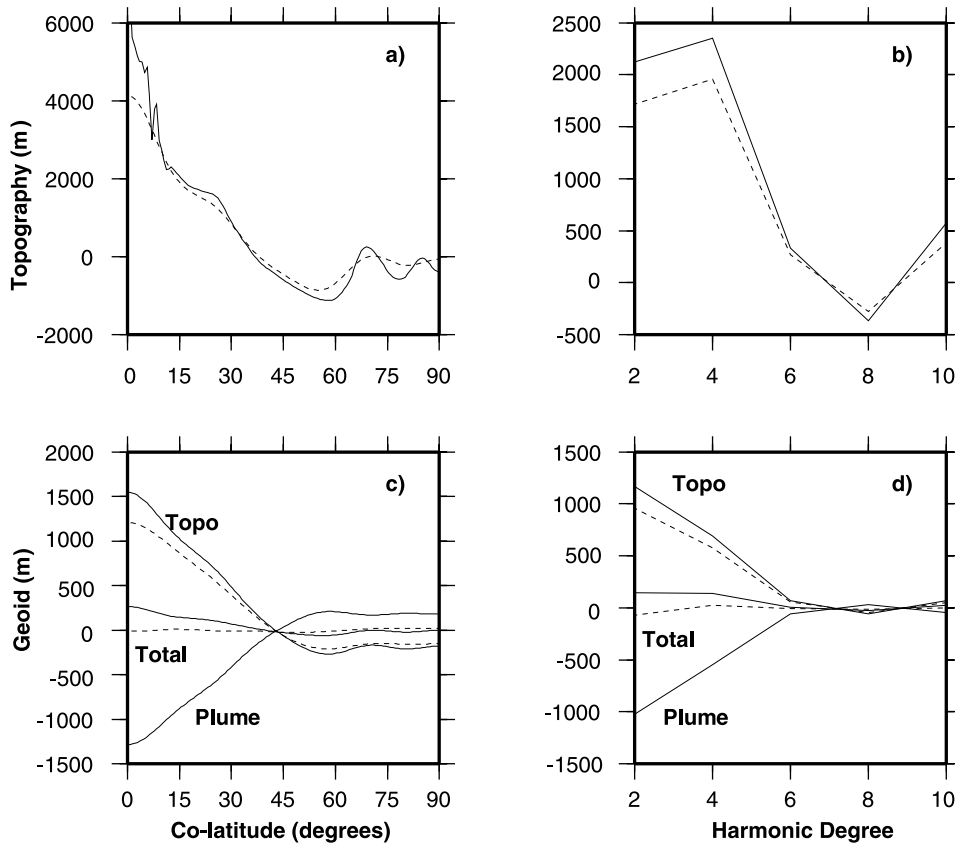


Figure 3. Dynamic topography (a, b) and geoid (c, d) from long-wavelength plume buoyancy for the case in Figure 1. Panels a and c are in spatial coordinates; panels b and d are plotted in terms of spherical harmonics. Solid and dashed lines are results before and after elastic filtering. The geoid due to topography includes the contribution from the CMB as well as the surface. $T_e = 147$ km, $\beta = 1.83$.

Figure 2. Each curve represents a different definition of T_e . The lines in Figure 2 are linear fits to the data.

3.3. Geoid and Topography

[22] Figures 3a and 3b show representative topographic profiles at the surface and their spectra for the case presented in Figure 1. We show the surface topography with (dashed line) and without (solid line) the elastic filtering effects. For this case with $T_e = 147$ km, the maximum topography above the plume is reduced from 5600 m to 4100 m after the filter is applied. The dynamic uplift extends to 40° from the plume center. The topography is dominated by components at degrees 2 and 4.

[23] Figures 3c and 3d show the geoid contributions from the surface and CMB topography, from the plume buoyancy, and the total geoid. The reduced surface topography has dramatic effects on the geoid. The unfiltered total geoid (solid line) shows a positive anomaly at long wavelengths and above the plume, although the magnitude of this anomaly is still much smaller than the observed values. The filtered geoid is reduced and the $\ell = 2$ component is negative.

[24] We now present geoid and topography for models with different parameters. Because, the observed geoid and topography associated with the Tharsis rise is well represented by only the few longest wavelengths [Zuber and Smith, 1997; Zhong and Roberts, 2003], we only present the

modeled topography and geoid at these wavelengths ($\ell \leq 4$). Figures 4a–4d show the dependence of the geoid and topography on T_e at degrees 2 and 4. In general the amount of dynamic topography increases with T_e . When T_e is high, the heat flow at the surface is low. This is often caused by high mantle viscosity which leads to high normal stress at the surface or dynamic topography. However, at low T_e , the opposite behavior is seen. A minimum in the dynamic topography is seen at $T_e \sim 115$ km and the topography actually increases as T_e drops below that (Figure 4a). These relatively high $\ell = 2$ topography results at low T_e are all from cases with either very low activation energy, or very high activation volume. Either property enhances the low viscosity layer below the stagnant lid, and the plume can spread out more easily, compared to the other cases. The power at degree 2 (e.g., Figure 1b) is increased and therefore more degree-2 topography is created.

[25] Before filtering, the geoid is in general larger, for larger T_e . However, the increase in geoid with T_e vanishes when the elastic filter is applied. The geoid is very small or negative for all values of T_e . Long-wavelength topography and geoid are highly correlated on Mars [McGovern *et al.*, 2002], and the ratio of geoid to topography, $R_{G/T}$ is also relatively high. At $\ell = 2$, the observed $R_{G/T} = 0.30$ [Zhong and Roberts, 2003]. The $R_{G/T}$ that would be generated by plume buoyancy is much smaller. As depicted in Figures 4e and 4f, $R_{G/T} < 0.09$ at degree 2 even without the elastic

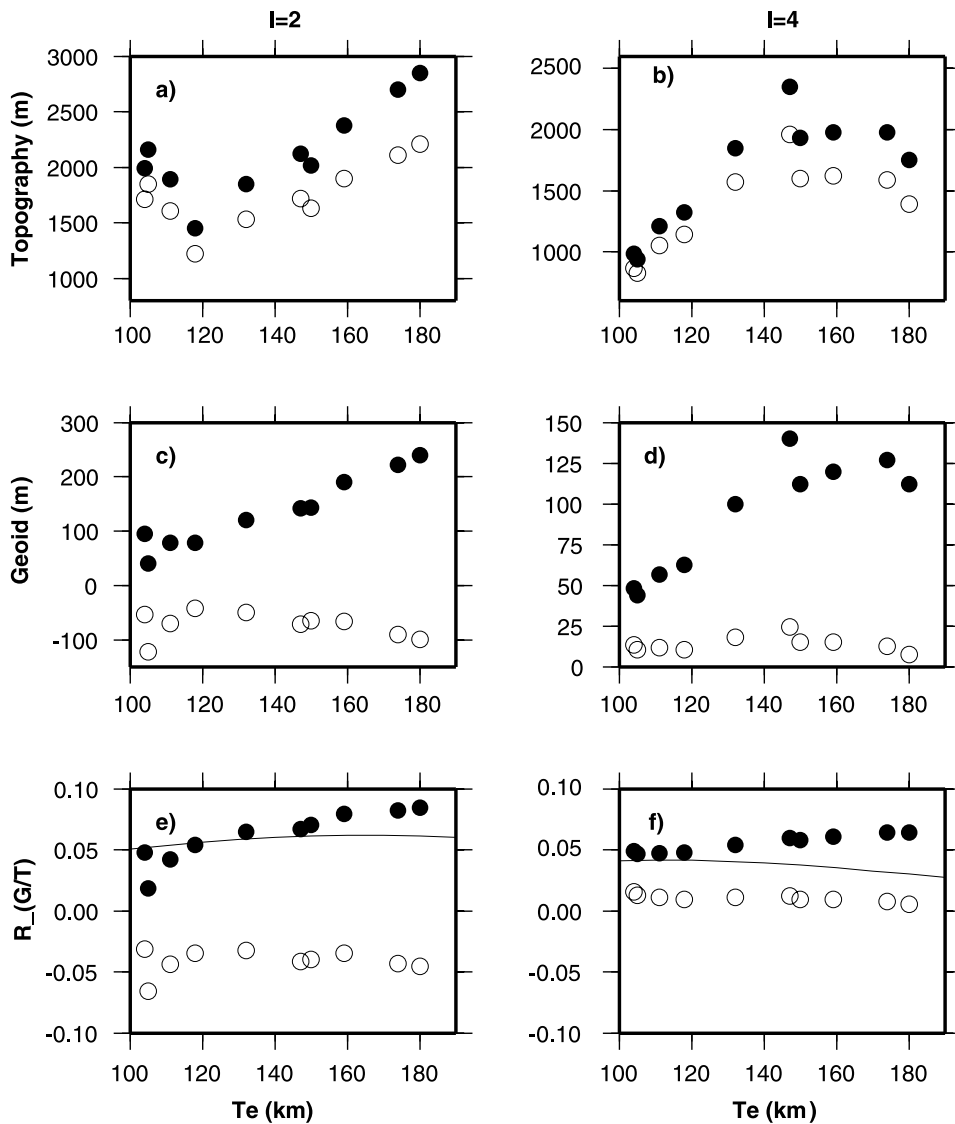


Figure 4. Dependence of dynamic topography (a, b), geoid (c, d) and $R_{G/T}$ (e, f) on T_e . Panels a, c, and e are for $\ell = 2$; panels b, d, and f are for $\ell = 4$. Solid and open circles are the results before and after the elastic filtering. The curved lines in panels e and f are the predictions from Zhong and Roberts [2003] for $\beta = 2$.

filtering. With an elastic lithosphere, the net geoid due to the plume is negative and thus so is $R_{G/T}$. At $\ell = 4$, $R_{G/T}$ is positive, but less than 0.03.

4. Discussion and Conclusions

[26] By formulating mantle convection models in a spherically axisymmetric geometry with temperature- and depth-dependent viscosity, we studied the plume-induced topography and gravity anomalies and their implications for the support of the Tharsis rise on Mars. We determined from the convection models the depth of the long-wavelength components of plume buoyancy, D_p , and the elastic thickness of the lithosphere, T_e , both of which affect the plume-induced topography and gravity. We found from ten models with different convective vigor and rheological parameters that T_e ranges from 100 km to 180 km and that the ratio of

D_p to T_e is approximately equal to 2. This ratio changes slightly if T_e is defined in different ways, but it remains relatively constant and close to 2. Our range of T_e is consistent with those inferred from modeling the gravity and topography data near young Martian volcanoes [Zuber *et al.*, 2001; McGovern *et al.*, 2002]. In all the cases we considered, the plume-induced geoid to topography ratio at wavelengths relevant to those of the Tharsis rise is significantly smaller than the observed value. In particular, at degree 2, the geoid to topography ratio is negative. This indicates that the present-day Tharsis gravity and topography anomalies cannot be dynamically supported by a mantle plume.

[27] By modeling the geoid to topography ratios from loading models with both internal loads (i.e., plume buoyancy) and surface loads, Zhong and Roberts [2003] indicated that a mantle plume can contribute no more than 15%

to the geoid, provided that T_e is <200 km and β is 3. The smaller β is, the smaller the geoid anomaly the plume produces. This is because at shallow depths, long-wavelength plume buoyancy produces negligibly small geoid [Zhong and Roberts, 2003]. That β is ~ 2 from our convection models in this study further strengthens their conclusion on the upper bounds for the plume-induced topography and geoid for the Tharsis rise. With $\beta = 2$, the loading models from Zhong and Roberts [2003] would suggest that the upper bounds for the possible contributions from a plume to the observed geoid should be further reduced to 5% at $\ell = 2$ and 11% at $\ell = 4$ [see Zhong and Roberts, 2003, Figure 3]. The loading models used in this study, however, consider an internal load distributed over depth. This model indicates that there is a negative geoid contribution from the plume at $\ell = 2$.

[28] Our results support the idea that the Tharsis anomalies result from surface loading of volcanic construction on an elastic lithosphere, which may have been placed as a result of giant volcanic events at the end of the Noachian, possibly related to the burst of a plume head [Zhong and Roberts, 2003]. However, we do not imply that there is no plume underneath Tharsis. The Tharsis region contains many recent lava flows, some as young as the late Amazonian [Tanaka et al., 1992]. There must be a heat source underneath Tharsis to produce the melt for this recent volcanism. Thermal plumes that may be residuals of the plume head events producing the Tharsis rise may provide the heat source for this recent volcanism.

[29] **Acknowledgments.** We would like to thank S. A. Hauck II, and C. Conrad for their careful reviews. This research is supported by NASA Grant NAG5-11224, the David and Lucile Packard Foundation and the Alfred P. Sloan Foundation.

References

- Hager, B. H., and M. A. Richards (1989), Long-wavelength variations in Earth's geoid: Physical models and dynamical implications, *Philos. Trans. R. Soc. London, Ser. A*, *328*, 309–327.
- Harder, H. (2000), Mantle convection and the dynamic geoid of Mars, *Geophys. Res. Lett.*, *27*, 301–304.
- Harder, H., and U. R. Christensen (1996), A one-plume model of Martian mantle convection, *Nature*, *380*, 507–509.
- Karato, S., and P. Wu (1993), Rheology of the upper mantle: A synthesis, *Science*, *260*, 771–778.
- Kiefer, W. S. (1997), Mantle plumes with temperature-dependent viscosity: Implications for interpretation of gravity anomalies on Venus (abstract), *Lunar Planet. Sci., XXVIII*, abstract 1758.
- King, S. D., and B. H. Hager (1994), Subducted slabs and the geoid: 1. Numerical experiments with temperature-dependent viscosity, *J. Geophys. Res.*, *99*, 19,843–19,852.
- McGovern, P. J., S. C. Solomon, D. E. Smith, M. T. Zuber, M. Simons, M. A. Wieczorek, R. J. Phillips, G. A. Neumann, O. Aharonson, and J. W. Head (2002), Localized gravity/topography admittance and correlation spectra on Mars: Implications for regional and global evolution, *J. Geophys. Res.*, *107*(E12), 5136, doi:10.1029/2002JE001854.
- Moresi, L., and M. Gurnis (1996), Constraints on the lateral strength of slabs from three-dimensional dynamic flow models, *Earth Planet. Sci. Lett.*, *138*, 15–28.
- Moresi, L., and V. S. Solomatov (1995), Numerical investigations of 2D convection with extremely large viscosity variations, *Phys. Fluids*, *7*, 2154–2162.
- Nimmo, F., and D. J. Stevenson (2000), Influence of early plate tectonics on the thermal evolution and magnetic field of Mars, *J. Geophys. Res.*, *105*, 11,969–11,979.
- Phillips, R. J., et al. (2001), Ancient geodynamics and global-scale hydrology on Mars, *Science*, *291*, 2587–2591.
- Reese, C. C., V. S. Solomatov, and J. R. Baumgardner (2002), Survival of impact-induced thermal anomalies in the Martian mantle, *J. Geophys. Res.*, *107*(E10), 5082, doi:10.1029/2000JE001474.
- Tanaka, K. L., D. H. Scott, and R. Greeley (1992), Global stratigraphy, in *Mars*, edited by H. H. Kieffer et al., pp. 345–382, Univ. of Ariz. Press, Tucson.
- Turcotte, D. L., R. J. Willemann, W. F. Haxby, and J. Norberry (1981), Role of membrane stresses in the support of planetary topography, *J. Geophys. Res.*, *86*, 3951–3959.
- Watts, A. B., J. H. Bodine, and N. M. Ribe (1980), Observations of the flexure and geological evolution of the Pacific Ocean basins, *Nature*, *283*, 532–537.
- Zhong, S. (2002), Effects of lithosphere on the long-wavelength gravity anomalies and their implications for the formation of the Tharsis rise on Mars, *J. Geophys. Res.*, *107*(E7), 5054, doi:10.1029/2001JE001589.
- Zhong, S., and J. H. Roberts (2003), On the support of the Tharsis rise on Mars, *Earth Planet. Sci. Lett.*, *214*, 1–9.
- Zhong, S., and M. T. Zuber (2001), Degree-1 mantle convection and the crustal dichotomy on Mars, *Earth Planet. Sci. Lett.*, *189*, 75–84.
- Zuber, M. T., and D. E. Smith (1997), Mars without Tharsis, *J. Geophys. Res.*, *102*, 28,673–28,685.
- Zuber, M. T., et al. (2001), Internal structure and early thermal evolution of Mars from Mars Global Surveyor topography and gravity, *Science*, *287*, 1788–1793.

J. H. Roberts, Department of Astrophysical and Planetary Sciences, University of Colorado, UCB 391, Boulder, CO 80309-0391, USA. (jhr@anquetil.colorado.edu)

S. Zhong, Department of Physics, University of Colorado, UCB 390, Boulder, CO 80309-0390, USA. (szhong@spice.colorado.edu)